Mn and Mo co-doped NiS nanosheets induces abundant Ni^{3+}-O bonds for efficient electro-oxidation of biomass

Pengfei Ren[a], Zixuan Wang[a], Wenchao Zhang[b], Fang Duan[a], Shuanglong Lu[a], Mingliang Du*[a], Han Zhu*[a]

a.   Key Laboratory of Synthetic and Biological Colloids, Ministry of Education, School of Chemical and Material Engineering, Jiangnan University, Wuxi, Jiangsu 214122, P. R. China. E-mail: zhysw@jiangnan.edu.cn; du@jiangnan.edu.cn.

b.   School of Chemistry and Life Sciences, Suzhou University of Science and Technology, Suzhou, 215009, Jiangsu, P. R. China.

Materials

Nickel nitrate hexahydrate (Ni(NO$_3$)$_2$·6H$_2$O, ≥97.5%), molybdenum acetylacetonate (C$_{10}$H$_{14}$MoO$_6$,), manganese acetylacetonate (C$_{15}$H$_{21}$MnO$_6$, ≥95%), thiourea (CH$_4$N$_2$S, AR), acetone (C$_3$H$_6$O, AR) and ethanol (C$_2$H$_6$O, AR) were purchased from Shanghai Macklin Biochemical Co., Ltd. Carbon paper (CP) was purchased from Shanghai Yuhong Chemical Technology Co., Ltd.

Pretreatment of CC

CP is first washed with 1M HCl, then rinsed with ultrapure water until neutral, subsequently washed three times with ethanol and acetone, and finally dried.

Preparation of MnMo-NiS

MnMo-NiS was synthesized through a one-step method. Solution A: 0.6 mmol Ni(NO$_3$)$_2$·6H$_2$O, 0.2 mmol C$_{10}$H$_{14}$MoO$_6$, and 0.1 mmol C$_{15}$H$_{21}$MnO$_6$ are mixed in 10 ml of ethanol and stirred for 20 minutes. Solution B: 1 mmol thiourea is added to 5 ml of ethanol and stirred for 20 minutes. Solutions A and B are then mixed and stirred for 10 minutes, and the mixture is placed in a Teflon-lined autoclave with a 1 × 2 cm² CP. The reaction is carried out at 180°C for 12 hours. After the reaction, the CP is washed three times with ethanol and ultrapure water, and then placed in a 60°C oven for 12 hours to obtain MnMo-NiS.

Preparation of NiS

NiS is synthesized using the same method as for Mn Mo-NiS, but instead of adding

precursors containing Mo and Mn, 0.9 mmol of nickel nitrate is used.

Materials characterizations

The field emission scanning electron microscope (FE-SEM, HITACHI S-4800) was used to acquire FE-SEM images at an accelerating voltage of 3 kV. The transmission electron microscope (TEM, JEM-2100 plus) was employed to record TEM images at an accelerating voltage of 200 kV. Bright-field and high-angle annular dark field scanning transmission electron microscope (STEM) images, as well as energy-dispersive X-ray spectroscopy (EDX) mapping images and line-scanning EDX spectra, were characterized using the Tecnai G2 F30S-Twin (Philips-FEI) at an accelerating voltage of 300 kV. X-ray diffraction (XRD) patterns were obtained with a Smartlab 9kW advance powder X-ray diffractometer (λ = 1.5406 Å) in the 2θ range of 20-80° with scan speeds of 0.5 or 10° min^{-1}, operating with a Cu Kα source at 40 kV and 40 mA. X-ray photoelectron spectroscopy (XPS) spectra were acquired using a Thermo Scientific K-Alpha, with an Al (mono) Kα source (1486.6 eV) operating at 12 kV and 6 mA. Binding energies were calibrated using C 1 s (284.8 eV) as the reference. Electrochemical Raman tests were conducted in a custom-made circular electrolytic cell. Ag/AgCl and Pt wire were used as the reference electrode (RE) and counter electrode (CE), respectively. The prepared electrocatalysts were dispersed on a glassy carbon electrode (GCE). The electrochemical processes were carried out in 1.0 M KOH + 0.1 M substrate, and controlled by a CHI660E electrochemical workstation. The Raman spectra were recorded with a Raman spectrometer (inVia) using a laser wavelength of 532 nm.

Electrochemistry characterizations

Electrochemical measurements were conducted at 25°C using a typical three-electrode system with 1.0 M KOH + 0.1 M substrate, employing a CHI660E electrochemical workstation. A saturated calomel electrode (SCE) and a graphite rod were used as the reference electrode (RE) and counter electrode (CE), respectively. The SCE was calibrated before each test. CP was cut into 1 × 1 cm² pieces and used as the working electrode (WE). The potential was converted to a reversible hydrogen electrode (RHE) using the equation E_{RHE} = E_{SCE} + 0.244 + 0.059 × pH. The chronoamperometry was used at specific voltages for product analysis of the electrolyte and durability testing. The open-circuit potential (OCP) measurement was performed in a three-electrode setup using 1 M KOH + 0.1 M substrate as the electrolyte.

Production characterizations

The products of HMFOR were analyzed by high-performance liquid chromatography (HPLC). Take 10 µL of the electrolyte from the 1M KOH + 0.1M HMF after electrolysis, add 10 µL of 0.5M H_2SO_4, and dilute to 1 mL. Analyze using a Shimadzu LC-20ADXR high-performance liquid chromatography system, equipped with an SPD-20A UV detector set to 265 nm, and a 4.6 mm × 150 mm Shim-pack GWS 5µm C18 column. The mobile phase consists of 5 mM ammonium formate and methanol in 7:3, with a column temperature of 40°C and a flow rate of 0.5 mL/min. Inject 5 µL of the sample for analysis. The products of EGOR and GLOR were analyzed by nuclear magnetic resonance (NMR). For each NMR measurement, 400 µL of electrolyte was used, with the addition of 100 µL D_2O and 100 µL of 0.1M dimethyl sulfoxide (DMSO) solution as an internal standard to analyze the liquid products. The Faraday efficiency and yield of HMF are calculated by eq(1), eq(2):

$$Faraday\ efficiency\ (\%) = \frac{n(FDCA, FA)}{\left[\dfrac{Charge}{n*F}\right]} (in\ EGOR\ and\ GLOR, n = 4, In\ HMFOR, n = 6)$$

(1)

$$Yield = \frac{n(FDCA, FA)}{1\ h \cdot 1\ cm^2}$$

(2)
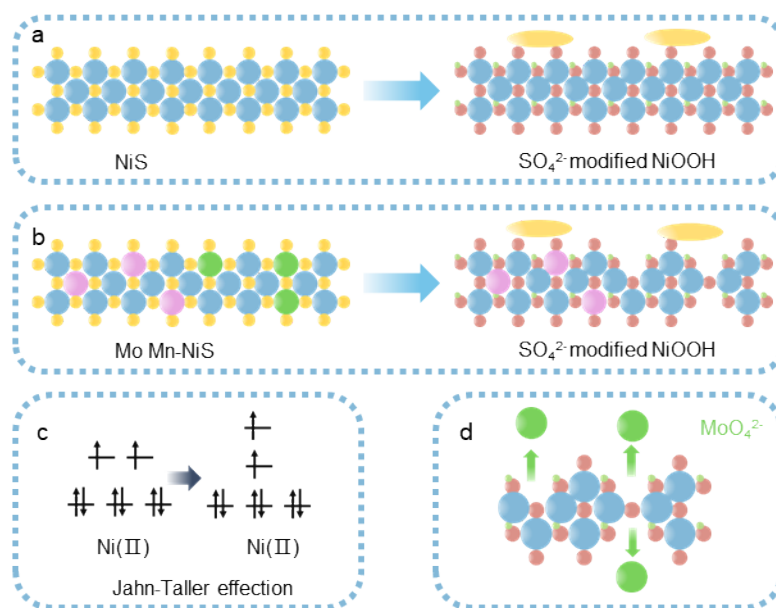
Figure S1. Schematic of the electro-oxidation of NiS (a) and MnMo-NiS (b). (c) Schematic of the energy level rearrangement of Ni^{2+}. (d) Schematic of the dissolution effect of MoO_4^{2-}.
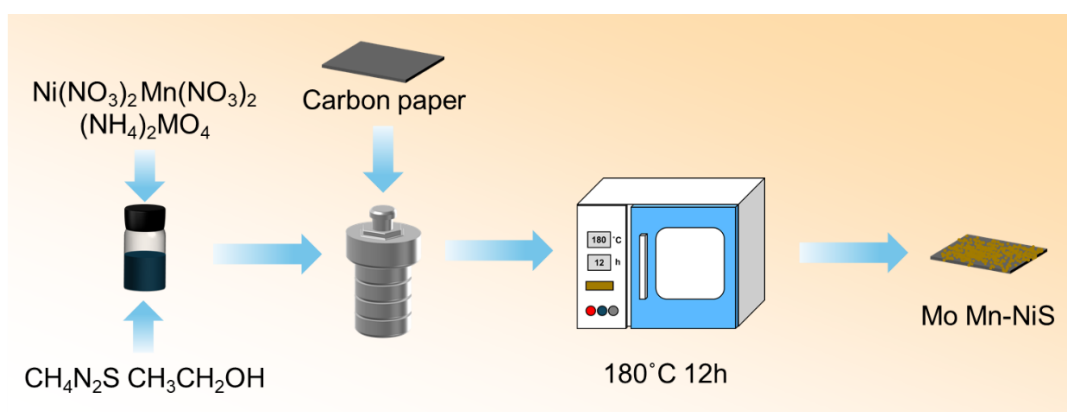
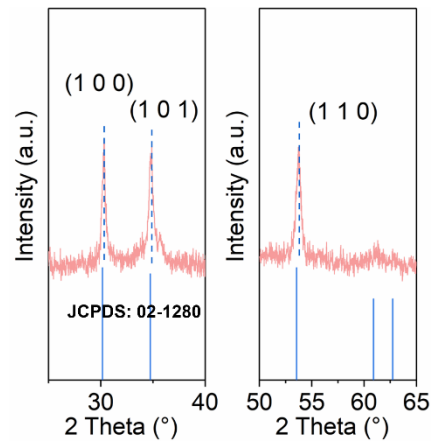**Figure S2**. Synthesis procedure of MnMo-NiS.

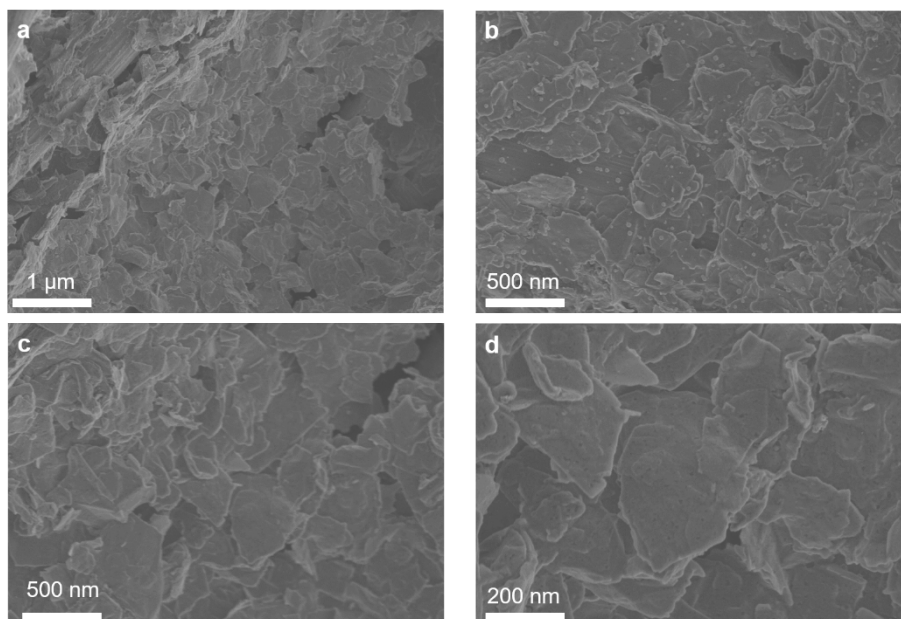**Figure S3**. XRD patterns of MnMo-NiS.

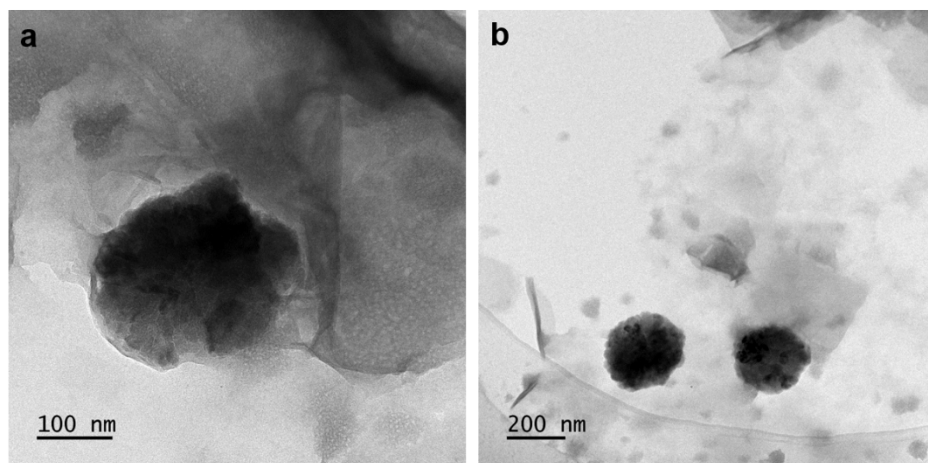**Figure S4.** (a-d) FE-SEM images of MnMo-NiS.
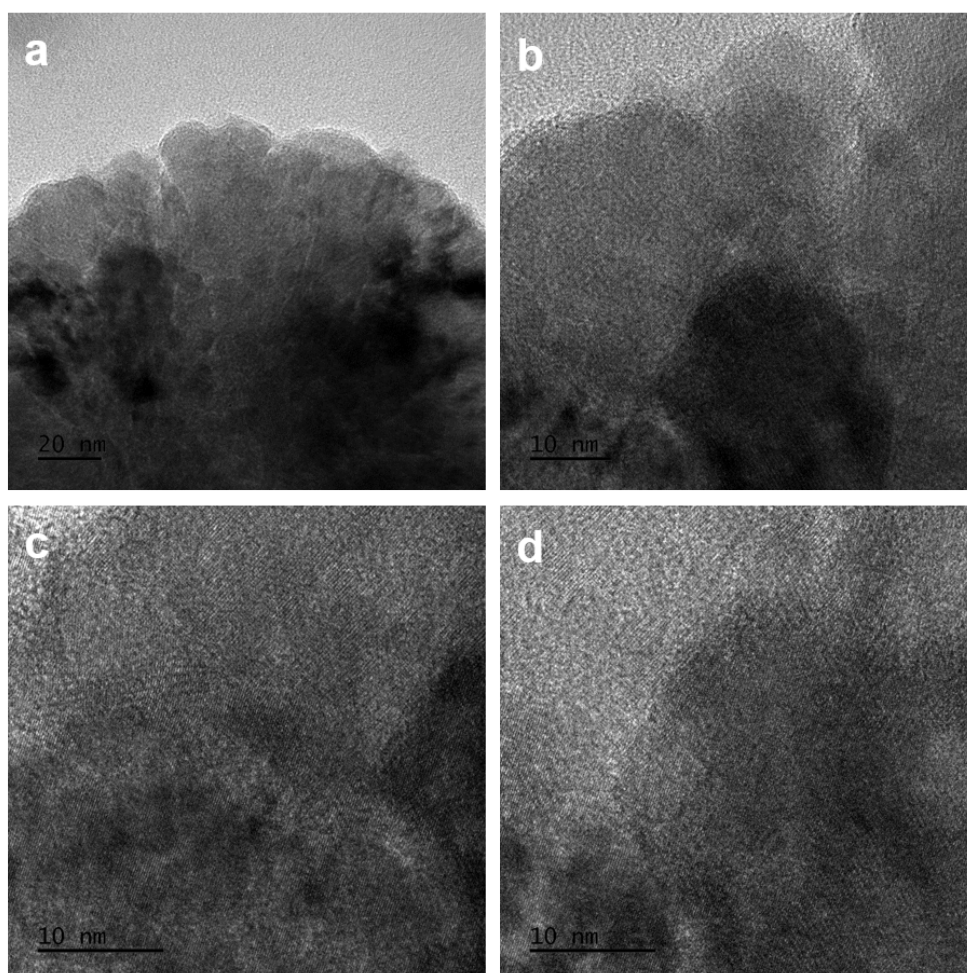
Figure S5. (a-d) TEM images of MnMo-NiS.
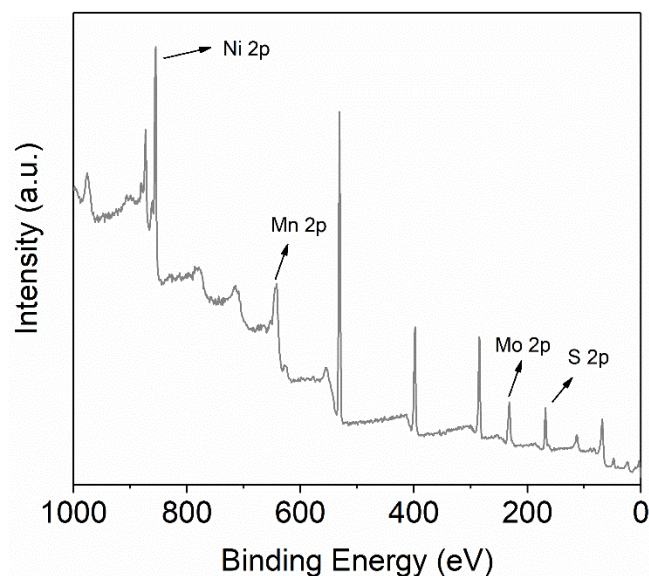

Figure S6. (a-d) HRTEM images of MnMo-NiS.
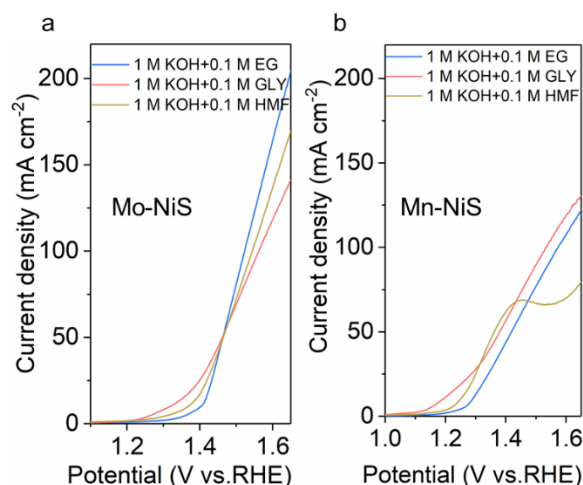
Figure S7. XPS survey spectrum of MnMo-NiS.

Figure S8. LSV curve of Mn-NiS (a) and Mo-NiS (b) obtained in 1 M KOH with 0.1 M EG, GLY and HMF, respectively.

To investigate the role of Mn and Mo in the reaction, LSV curves were measured for Mn-NiS and Mo-NiS (Figure S8). At 1.5 V vs. RHE, the Mo-NiS achieve the current densities of 78, 74, and 74 mA cm-2 for EGOR, GLOR, and HMFOR while the Mn-NiS reach the current density of 75, 86, and 69 mA cm-2, respectively, which were higher than those of NiS (29, 50 and 75 mA-2). Specifically, MnMo-NiS exhibits the current densities of 168, 177, and 134 mA cm-2 at 1.5 V (Figure 2c), which are substantially higher than those control samples, demonstrating that the co-doping with Mn and Mo is an effective method to improve the activity of NiS. The results indicate that compared to pure NiS, doping with either Mn or Mo alone could moderately enhance the EGOR and GLOR activities, but the improvement in HMFOR activity is limited. However, co-doping with Mn and Mo significantly increases the current density and

activity across all three reactions. Therefore, we propose that the role of Mn and Mo is to modify the electronic structure of NiS, thereby significantly improving the EGOR, GLOR, and HMFOR performance of NiS. The co-doping of Mn and Mo induces the Jahn-Teller effect in octahedral NiS, leading to rearrangement of the energy levels.
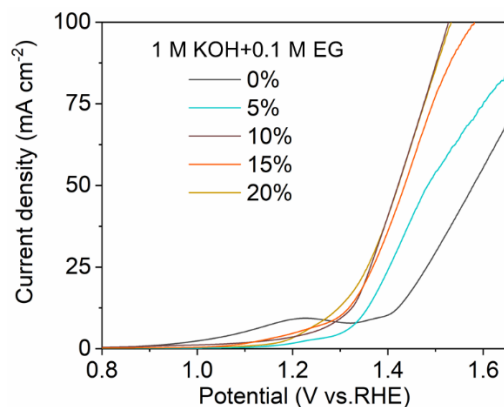

Figure S9. LSV curves of NiS doped with 0-20% amounts of Mn.

The NiS samples doped with varying molar concentrations of Mn or Mo were prepared and their impact on EGOR was evaluated. As shown in Figure S9, Mn doping causes an earlier shift in the EGOR potential of NiS. However, at concentrations exceeding 10%, the change in current density becomes negligible. This phenomenon may be attributed to the high Mn content, where excess Mn fails to fully integrate into the NiS lattice and instead forms a separate manganese sulfide phase. Since manganese sulfide exhibits minimal catalytic activity, the overall activity remains nearly unchanged.
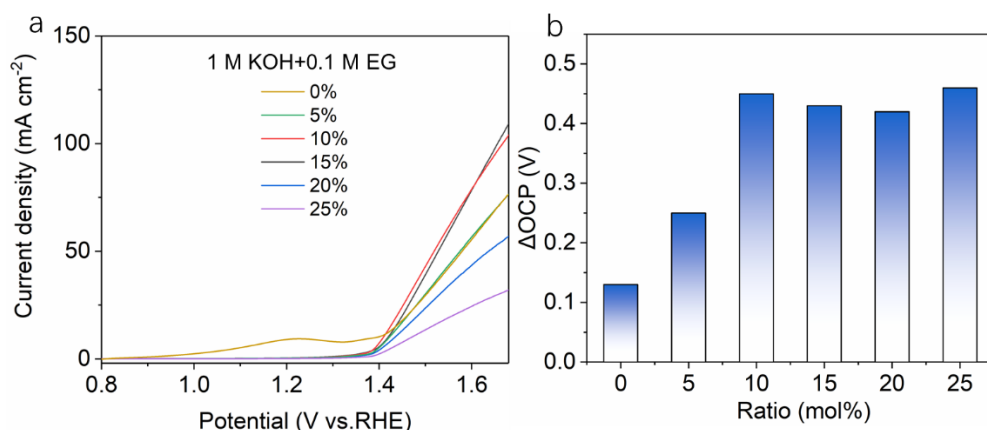
Figure S10. LSV curves (a) and ΔOCP (b) of NiS doped with 0-25% amounts of Mo.

As shown in Figure S10, at doping levels between 0–5%, there is a slight increase in current density, while at 10%, the current density reaches near-maximum values. Between 10% and 15%, the current density remains relatively unchanged, and beyond

15%, it begins to decline. This suggests that Mo doping accelerates the reaction rate. The enhancement in reaction rate may be linked to improved reactant adsorption. To further analyze the effects of Mo doping, the change in open-circuit potential (ΔOCP) before and after the addition of nucleophilic reagents was measured. As shown in Figure R4b, the ΔOCP increases with increasing Mo concentrations, but plateaus when the doping level reaches 10%. This indicates that at lower doping levels, leached Mo enhances reactant adsorption by creating metal vacancies. However, at higher Mo concentrations, phase separation of Mo occurs, with the segregated Mo having little impact on the reaction. Additionally, excessive Mo reduces the number of active Ni sites, leading to a decline in the reaction rate.
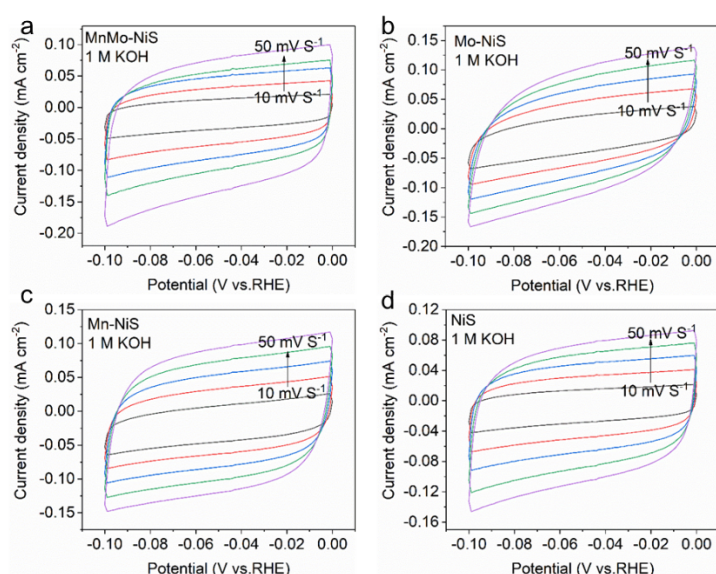
Figure S11. CV curves of MnMo-NiS (a), Mn-NiS (b), Mo-NiS (c), and NiS (d).
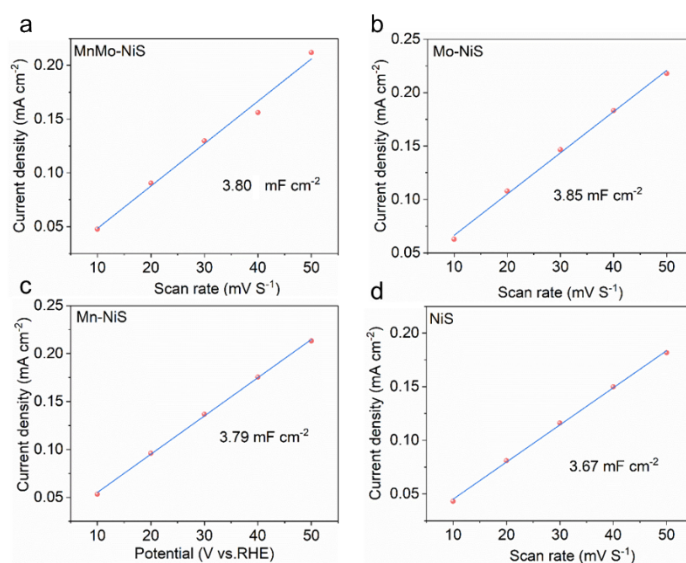
Figure S12. C_{dl} of MnMo-NiS (a), Mn-NiS (b), Mo-NiS (c), and NiS (d).
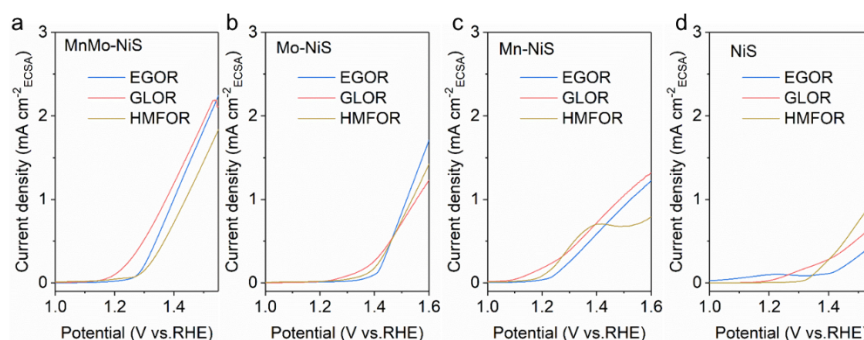
Figure S13. The ECSA-normalized LSV curves of MnMo-NiS (a), Mn-NiS (b), Mo-NiS (c), and NiS (d).

The C_{dl} values for MnMo-NiS, Mn-NiS, Mo-NiS, and NiS are nearly identical (3.80, 3.85, 3.79, and 3.67 mF cm^{-2}, respectively), indicating that Mn and Mo doping does not significantly affect the electrochemically active surface area. The ECSA-normalized LSV curves demonstrate that MnMo-NiS exhibits significantly higher current densities for EGOR, GLOR, and HMFOR (1.76, 1.77, and 1.48 mA cm^{-2} at 1.5 V) compared to Mn-NiS (0.91, 1.02, and 0.82 mA cm^{-2}), Mo-NiS (0.83, 0.81, and 0.81 mA cm^{-2}), and NiS (0.33, 0.46, and 0.74 mA cm^{-2}). This suggests that co-doping notably enhances the intrinsic activity of NiS (Figures S11-S13).
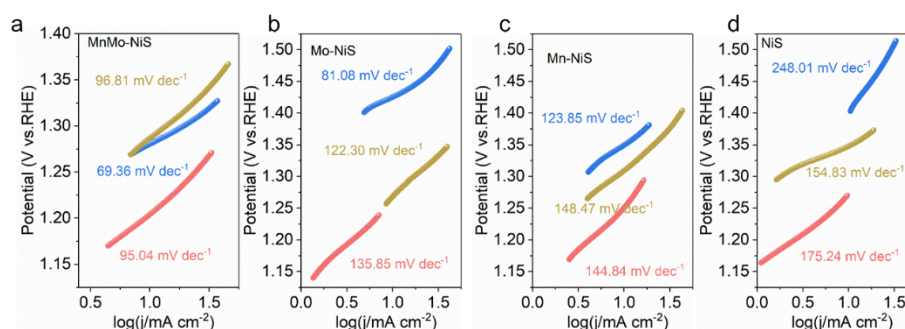
Figure S14. Tafel slope of MnMo-NiS (a), Mn-NiS (b), Mo-NiS (c), and NiS (d).

As shown in Figure S14, the Tafel slopes of MnMo-NiS, Mn-NiS, Mo-NiS, and NiS were measured. MnMo-NiS exhibits lower Tafel slopes (69.36, 95.34, and 96.81 mV dec^{-1}) compared to Mn-NiS (123.85, 144.84, and 148.47 mV dec^{-1}), Mo-NiS (81.08, 135.85, and 133.30 mV dec^{-1}), and NiS (248.01, 175.24, and 154.83 mV dec^{-1}). This indicates that MnMo-NiS demonstrates superior kinetic activity, underscoring the fact that dual metal doping significantly enhances the kinetic performance of the reaction.
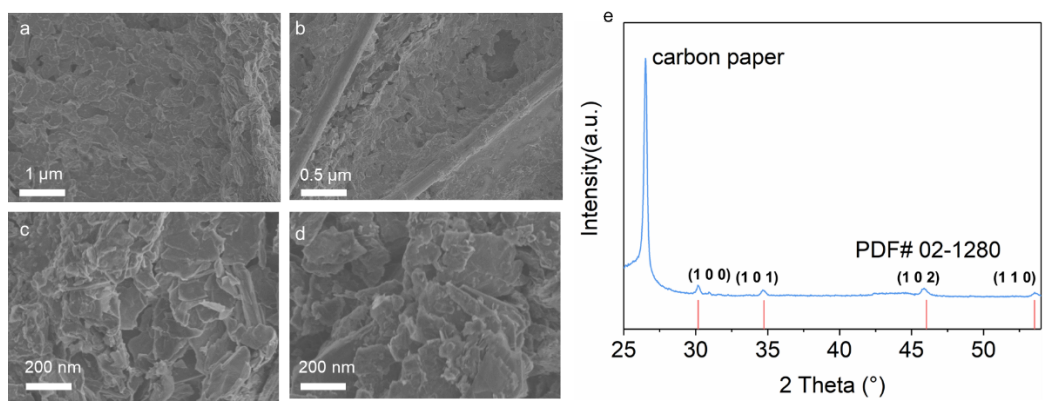
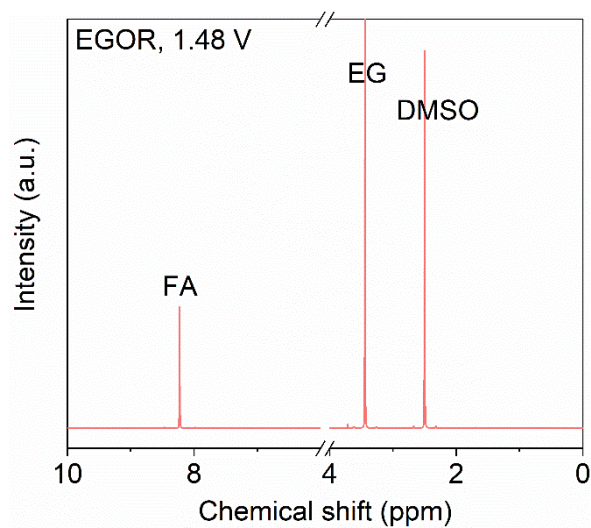**Figure S15.** SEM image (a-c) and XRD pattern (e) of MnMo-NiS after stability testing.

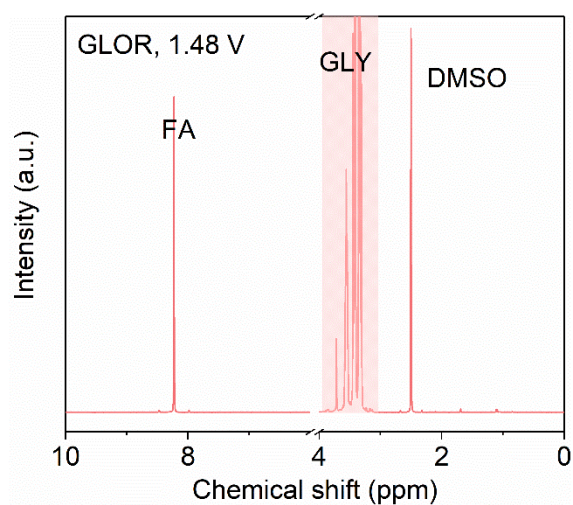**Figure S16.** ^{1}H NMR spectra of EGOR on MnMo-NiS at 1.48 V.

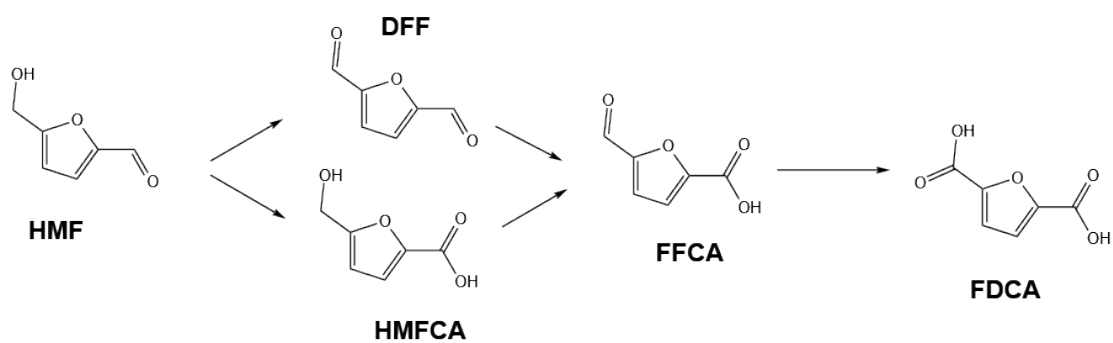**Figure S17.** ^{1}H NMR spectra of GLOR on MnMo-NiS at 1.48 V.
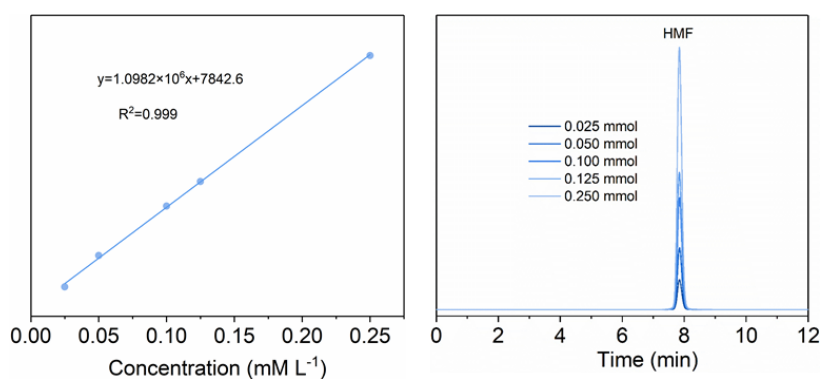
Figure S18. Reaction pathway diagram of HMFOR.

y=1.0982×10⁶x+7842.6

$y = 1.0982 \times 10^{6}x + 7842.6$

$R^2 = 0.999$

Figure S19. Standard curve graph of HMF.

$y = 961793.05x + 5664.21$

$R^2 = 0.998$
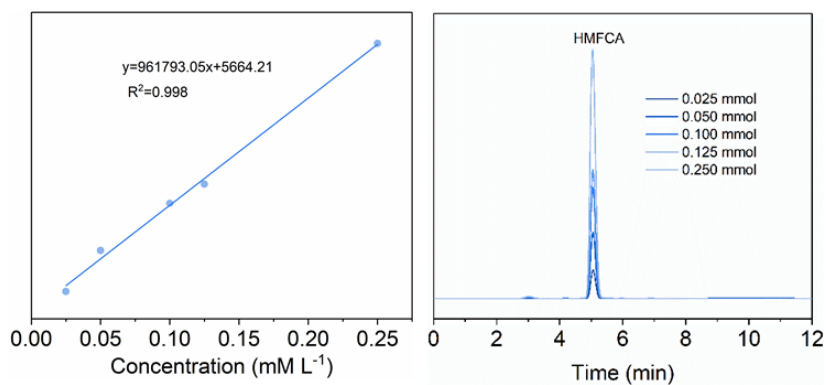
Figure S20. Standard curve graph of HMFCA.
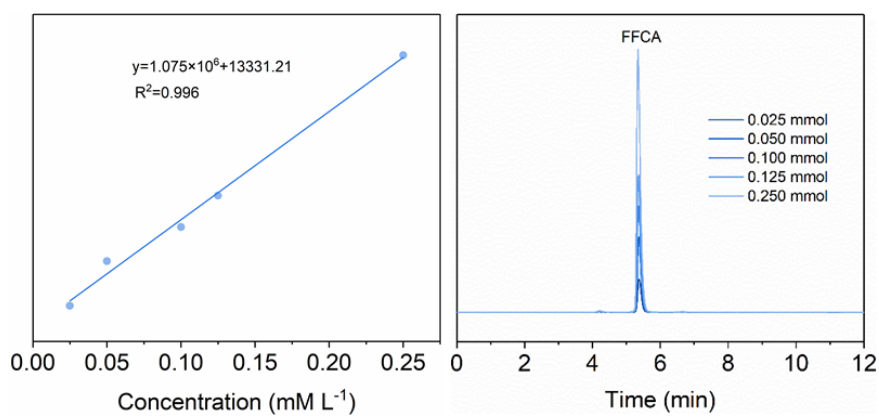
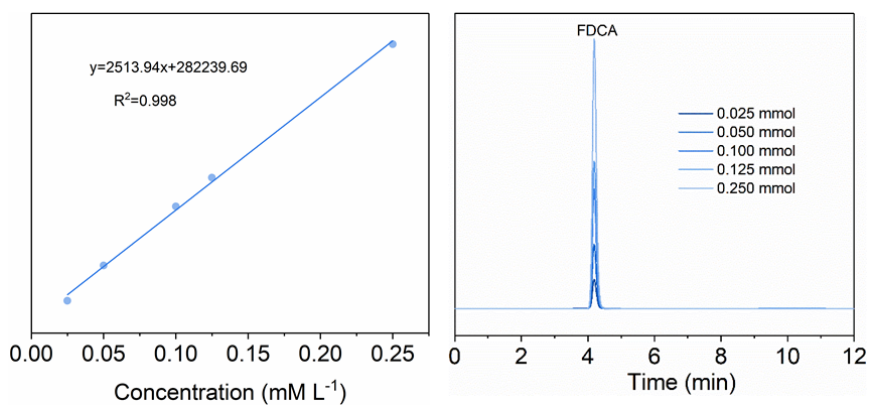**Figure S21.** Standard curve graph of FFCA.

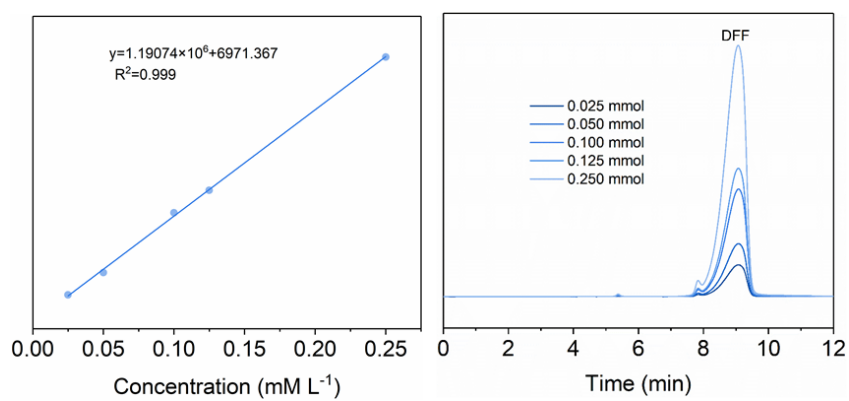**Figure S22.** Standard curve graph of FDCA.

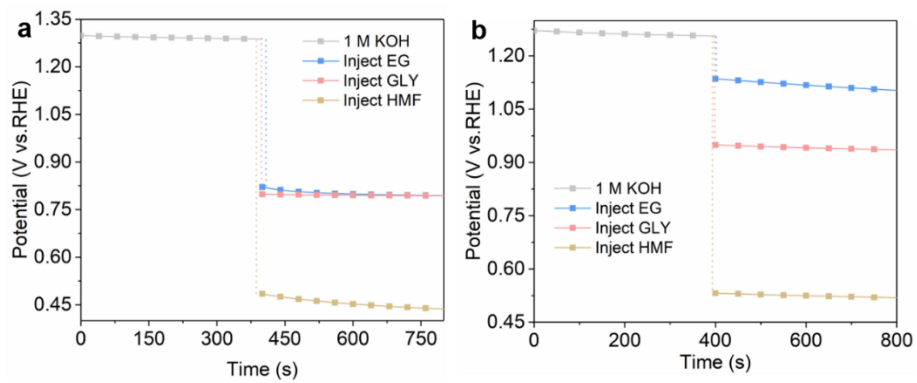**Figure S23.** Standard curve graph of DFF.

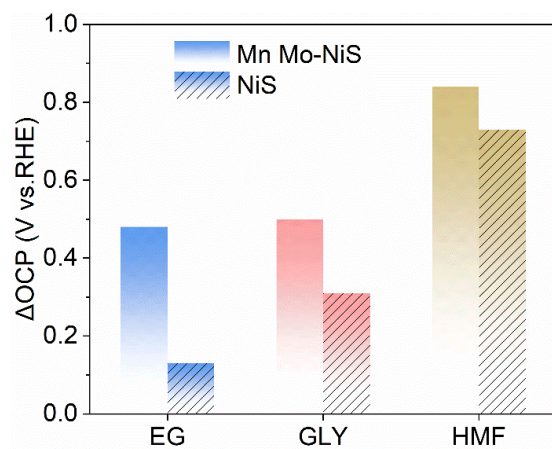**Figure S24.** OCP diagrams of MnMo-NiS (a) and NiS (b).

Figure S25. Comparison of OCP of MnMo-NiS and NiS in EGOR, GLOR, and HMFOR.